ORIGINAL ARTICLE

Open Access

CrossMark

Closed-Form Modeling and Analysis of an XY Flexure-Based Nano-Manipulator

Yan-Ding Qin[1*] , Xin Zhao[1], Bijan Shirinzadeh[2], Yan-Ling Tian[3] and Da-Wei Zhang[3]

Abstract

Flexure-based mechanisms are widely utilized in nano manipulations. The closed-form statics and dynamics modeling is difficult due to the complex topologies, the inevitable compliance of levers, the Hertzian contact interface, etc. This paper presents the closed-form modeling of an XY nano-manipulator consisting of statically indeterminate symmetric (SIS) structures using leaf and circular flexure hinges. Theoretical analysis reveals that the lever's compliance, the contact stiffness, and the load mass have significant influence on the static and dynamic performances of the system. Experiments are conducted to verify the effectiveness of the established models. If no piezoelectric actuator (PEA) is installed, the influence of the contact stiffness can be eliminated. Experimental results show that the estimation error on the output stiffness and first natural frequency can reach 2% and 1.7%, respectively. If PEAs are installed, the contact stiffness shows up in the models. As no effective method is currently available to measure or estimate the contact stiffness, it is impossible to precisely estimate the performance of the overall system. In this case, the established closed-form models can be utilized to calculate the bounds of the performance. The established closed-form models are widely applicable in the design and optimization of planar flexure-based mechanisms.

Keywords: Flexure-based mechanism, Statically indeterminate structure, Dynamics, Lever mechanism, Piezoelectric actuator

1 Introduction

The integrations of piezoelectric actuators (PEAs) and flexure-based mechanisms have been widely utilized in nano-positioning and manipulations [1–5]. On the one hand, the shape of a PEA changes if charge or voltage is exerted, and thus generating sub-nanometer resolution actuation. However, PEAs suffer from the inherent hysteresis and creep nonlinearities [6–8]. Many feedforward and feedback methodologies have been proposed to compensate for the hysteresis and creep nonlinearities of PEAs [9, 10]. On the other hand, flexure-based mechanisms are capable of transmitting high-precision motions via the elastic deformations of the flexure hinges, making it ideal in building the transmission chains for PEAs [11, 12]. Widely utilized flexure hinge profiles include circular [13–16] and leaf [17, 18].

A single flexure hinge can be treated as a revolute joint during micro- and nano-scale motions. In literature, many analytical and empirical models have been established for the compliance/stiffness of a single flexure hinge [19–21]. In order to improve the performance, multiple flexure hinges are generally combined in various configurations, such as the parallelograms [22–24] and the statically indeterminate symmetric (SIS) structures [25]. In these structures, it is common to treat the flexure hinges as flexible, and all the other components as rigid. Considering the widely-utilized lever mechanism as an example, the lever is frequently assumed to be rigid [26, 27] so as to facilitate the design and modeling processes. However, this assumption may increase the estimation error of the analytical model, especially when the lever is long or the compliance of the lever is not negligible.

A PEA is brittle and very weak when subjected to large lateral forces or torques. As a result, a PEA is not allowed to be firmly fixed to the mechanism during the installation. Many commercial PEAs use ball tips to eliminate the bending torques. In this case, a Hertzian contact

*Correspondence: qinyd@nankai.edu.cn
[1] Institute of Robotics and Automatic Information System (Tianjin Key Laboratory of Intelligent Robotics), Nankai University, Tianjin 300350, China
Full list of author information is available at the end of the article

Qin *et al. Chin. J. Mech. Eng.* (2018) 31:7

Page 2 of 11

interface forms between the tip and the mechanism. One significant drawback of Hertzian contact is its low contact stiffness that consumes large portion of the PEA's displacement. The contact stiffness is highly dependent on the material properties and the contact status. Currently, there is no effective and reliable model to estimate the contact stiffness. Thus, the contact stiffness is frequently identified from the measured data [2].

As a flexure-based mechanism is generally light and compact, its performance is likely to be affected by the load mass, including the sensors, end-effectors, fixtures, and other accessories installed on the mechanism. The load mass increases the effective mass and moment of inertia of the system, leading to a slow response. Thus, the influence of the load mass should be taken into consideration in the design and modeling of flexure-based mechanisms.

This paper presents the closed-form modeling of an XY flexure-based nano-manipulator developed in our previous work [28]. In this nano-manipulator, the flexure hinges are arranged in SIS configurations to transmit linear or angular motions. Analytical modeling reveals that the lever's compliance significantly increases the estimation error. Thus, a threshold is proposed to determine whether the lever's compliance can be neglected or not. Subsequently, a systematic modeling methodology is established to investigate the behavior of the nano-manipulator during linear and angular motions. Experimental results show that the modeling accuracy is significantly improved if the influence of the lever's compliance, the contact stiffness, and the load mass is taken into consideration.

2 Design of the XY Nano-manipulator

An XY flexure-based nano-manipulator was developed for nano manipulation tasks in our previous work [28]. The schematic diagram and the geometric parameters of the nano-manipulator are presented in Figure 1, where a central platform is connected to four rigid linkages (consecutively labeled as linkage 1–4) and then to the fixed frame through leaf springs. The nano-manipulator is symmetric in the x- and y-axes, thus attenuating thermally induced errors and guaranteeing uniform characteristics. In each axis, the displacement of a PEA (P-843.30 from Physik Instrumente) is magnified by a lever mechanism. Ball tip is selected to form a Hertzian contact interface so as to protect the PEA against the lateral forces and torques. Leaf and right circular flexure hinges are adopted in the manipulator. These flexure hinges are arranged into four different groups, namely Structure I-IV (labeled as I-IV in Figure 1). Except for Structure IV, the other structures are SIS structures with "clamped-clamped" boundary conditions. Experimental

results showed that the cross-axis coupling ratio of the nano-manipulator is below 1% [28].

3 Characteristics of the SIS Structures

3.1 In-plane Compliance of a Single Flexure Hinge

Leaf and right circular flexure hinges are utilized in the nano-manipulator. As illustrated in Figure 2, the geometric parameters are the hinge length $2L_0$ and the minimum thickness t. The shape functions of these hinges are defined in Eqs. (1) and (2), respectively:

$$y(x) = t/2, \tag{1}$$

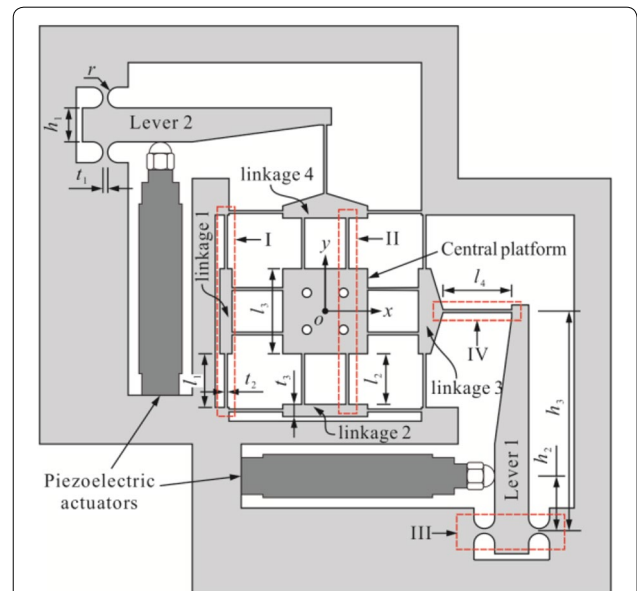$$y(x) = r + t/2 - r\sqrt{1 - x^2/r^2}, \quad x \in [-L_0, L_0], \tag{2}$$

Figure 1 Schematic diagram of the nano-manipulator. t_1, t_2: Minimal thickness of circular and leaf flexures, $t_1 = 0.58$, $t_2 = 0.44$, t_3: Thickness of linkages, $t_3 = 4$, r: Radius of the circular flexure hinge, $r = 3.41$, t_1, t_2, t_3: Parameters of the lever mechanism, $h_1 = 11.1$, $h_2 = 18$, $h_3 = 72$, l_1, l_2, l_4: Length of leaf flexures, $l_1 = 17.61$, $l_2 = 16.61$, $l_4 = 22.39$, l_3: Width of the central platform, $l_3 = 27.78$, d: Out-of-plane depth of the nano-manipulator, $d = 20$.
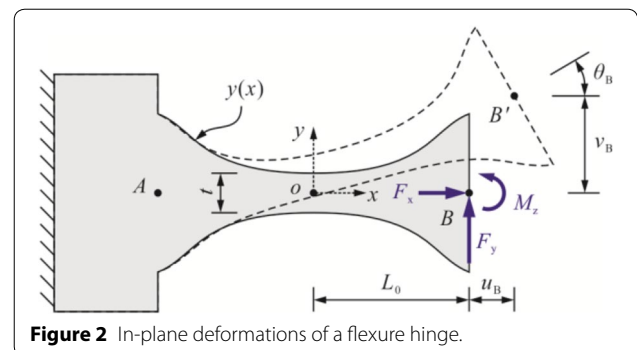

Figure 2 In-plane deformations of a flexure hinge.

where r is the radius of the circular profile, and for the right-circular flexure hinge, $r = L_0$.

As shown in Figure 2, the in-plane loads of the flexure hinge are the moment about the z-axis (M_z) and two forces in the x- and y-axes (F_x and F_y). The angular deflection about the z-axis and the linear deflections in the x- and y-axes are denoted as θ_B, u_B, and v_B, respectively. The bending moment $M_z(x)$ and shear force $Q(x)$ generated at position x may be written as

$$\begin{cases} M_z(x) = M_z + F_y(L_0 - x), \\ Q_y(x) = -F_y. \end{cases} \tag{3}$$

In the x-axis, the linear deflection at point B is defined by the following equation:

$$u_B = \int_{-L_0}^{L_0} \frac{F_x}{EA(x)} dx = \frac{F_x}{2Ed} \int_{-L_0}^{L_0} \frac{1}{y(x)} dx = F_x P_1, \tag{4}$$

where E is the Young's modulus, $A(x) = 2dy(x)$ is the cross sectional area of the hinge, and

$$P_1 = \frac{1}{2Ed} \int_{-L_0}^{L_0} \frac{1}{y(x)} dx.$$

Subsequently, the angular deflection of point B about the z-axis can be modeled as

$$\theta_B = \int_{-L_0}^{L_0} \frac{M_z(x)}{EI_z(x)} dx = \frac{3(M_z + F_y L_0)}{2Ed} \int_{-L_0}^{L_0} \frac{1}{y^3(x)} dx$$
$$= (M_z + F_y L_0) P_2, \tag{5}$$

where $I_z(x) = 2dy^3(x)/3$ is the second moment of area with respect to z-axis, and

$$P_2 = \frac{3}{2Ed} \int_{-L_0}^{L_0} \frac{1}{y^3(x)} dx.$$

Timoshenko beam theory is utilized to calculate the linear deflection in y-axis:

$$v_B = \int_{-L_0}^{L_0} \theta(x) dx - \int_{-L_0}^{L_0} \frac{Q(x)}{\kappa GA(x)} dx$$
$$= L_0 \theta_B + \frac{3F_y}{2Ed} \int_{-L_0}^{L_0} \frac{x^2}{y^3(x)} dx + F_y \frac{E}{\kappa G} P_1$$
$$= L_0 (M_z + F_y L_0) P_2 + F_y P_3 + F_y \frac{E}{\kappa G} P_1, \tag{6}$$

where $\theta(x)$ denotes the angular deflection at position x, G is the shear modulus, κ is the Timoshenko shear coefficient, and

$$P_3 = \frac{3}{2Ed} \int_{-L_0}^{L_0} \frac{x^2}{y^3(x)} dx.$$

For hinges with a rectangular cross section, $\kappa = 5/6$. Eqs. (4)–(6) can be rewritten into a matrix form:

$$\begin{pmatrix} u_B \\ v_B \\ \theta_B \end{pmatrix} = \begin{pmatrix} P_1 & 0 & 0 \\ 0 & \frac{E}{\kappa G} P_1 + L_0^2 P_2 + P_3 & L_0 P_2 \\ 0 & L_0 P_2 & P_2 \end{pmatrix} \begin{pmatrix} F_x \\ F_y \\ M_z \end{pmatrix}$$
$$= C \begin{pmatrix} F_x \\ F_y \\ M_z \end{pmatrix}, \tag{7}$$

where matrix C is defined as the in-plane compliance matrix of the flexure hinge.

In this paper, P_1–P_3 are only dependent on the geometric parameter of the hinge, and thus they are named as fundamental integrations.

3.2 Stiffness Modeling of the SIS Structures

Structure I-III can be schematically illustrated in Figure 3. It is obvious that static indeterminacy causes axial tension in lateral deformations, resulting in nonlinear load-deflection relationship. However, the deflection of a flexure-based mechanism is very small when compared to the dimension of the mechanism. Thus, the above structural nonlinearity can be treated as negligible [25]. This is also adopted in this paper.

The reaction forces and moments of the SIS structure are defined in Figure 3. The static equilibrium conditions lead to the following equations:

$$\begin{cases} F_x - F_{Ax} + F_{Bx} = 0, \\ F_y + F_{Ay} + F_{By} = 0, \\ M_z - M_{Az} + M_{Bz} - (F_{Ay} - F_{By})(2L_0 + L_1) = 0. \end{cases} \tag{8}$$

There are six unknown variables in the above equations. For this statically indeterminate problem, the reactions of the structure can be solved using the flexibility method. If we remove the constraints from point B and treat the reactions F_{Bx}, F_{By}, and M_{Bz} as additional loads, the original statically indeterminate structure can be transformed into a statically determinate structure. The transformed structure is equivalent to the original structure only when the deflections of the transformed structure at point B are the same as the original structure. As a result, another three equations are derived:
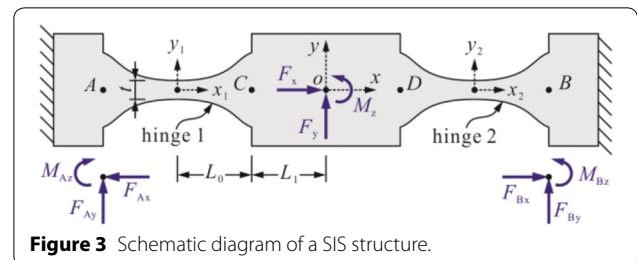

Figure 3 Schematic diagram of a SIS structure.

Qin *et al. Chin. J. Mech. Eng.* (2018) 31:7

Page 4 of 11

$$
\begin{pmatrix} u_B \\ v_B \\ \theta_B \end{pmatrix} = \overbrace{\begin{pmatrix} 1 & 0 & 0 \\ 0 & 1 & 2L_{01} \\ 0 & 0 & 1 \end{pmatrix} C \begin{pmatrix} F_x + F_{Bx} \\ F_y + F_{By} \\ M_z + M_{Bz} + F_y L_1 + 2F_{By}L_{01} \end{pmatrix}}^{\text{contribution of hinge 1}}
$$

$$
+ \overbrace{C \begin{pmatrix} F_{Bx} \\ F_{By} \\ M_{Bz} \end{pmatrix}}^{\text{contribution of hinge2}} = \begin{pmatrix} 0 \\ 0 \\ 0 \end{pmatrix},
\tag{9}
$$

where $L_{01} = L_0 + L_1$.

Linear superposition is used to facilitate the calculation, and *contribution of hinge* 1 (or 2) refers to the deflections of point B when only hinge 1 (or 2) is treated as flexible. Utilizing Eqs. (8) and (9), we obtain the reaction forces and moments as below:

$$
\begin{cases}
F_{Ax} = \frac{1}{2}F_x, \quad F_{Bx} = -\frac{1}{2}F_x, \\
F_{Ay} = -\frac{1}{2}F_y + \frac{1}{2}\frac{L_{01}P_2}{\frac{E}{\kappa G}P_1 + L_{01}^2 P_2 + P_3}M_z, \\
F_{By} = -\frac{1}{2}F_y - \frac{1}{2}\frac{L_{01}P_2}{\frac{E}{\kappa G}P_1 + L_{01}^2 P_2 + P_3}M_z, \\
M_{Az} = \frac{L_0}{2}F_y + \frac{1}{2}\frac{\frac{E}{\kappa G}P_1 - L_0 L_{01}P_2 + P_3}{\frac{E}{\kappa G}P_1 + L_{01}^2 P_2 + P_3}M_z, \\
M_{Bz} = \frac{L_0}{2}F_y - \frac{1}{2}\frac{\frac{E}{\kappa G}P_1 - L_0 L_{01}P_2 + P_3}{\frac{E}{\kappa G}P_1 + L_{01}^2 P_2 + P_3}M_z.
\end{cases}
\tag{10}
$$

Similarly, we can obtain the deflections at point O using the linear superposition method, as shown below:

$$
\begin{pmatrix} u_O \\ v_O \\ \theta_O \end{pmatrix} = \begin{pmatrix} 1 & 0 & 0 \\ 0 & 1 & l_1 \\ 0 & 0 & 1 \end{pmatrix} C \begin{pmatrix} F_x + F_{Bx} \\ F_y + F_{By} \\ M_z + M_{Bz} + F_y l_1 + 2F_{By}L_{01} \end{pmatrix}
$$

$$
= \begin{pmatrix} \frac{P_1}{2} & 0 & 0 \\ 0 & \frac{\frac{E}{\kappa G}P_1 + P_3}{2} & 0 \\ 0 & 0 & \frac{(\frac{E}{\kappa G}P_1 + P_3)P_2}{2[\frac{E}{\kappa G}P_1 + L_{01}^2 P_2 + P_3]} \end{pmatrix} \begin{pmatrix} F_x \\ F_y \\ M_z \end{pmatrix}.
\tag{11}
$$

Subsequently, the in-plane stiffness of the SIS structure can be derived from Eq. (11):

$$
\begin{cases}
k_L = F_x / u_O = 2/P_1, \\
k_T = F_y / v_O = 2 \big/ \left(\frac{E}{\kappa G}P_1 + P_3 \right), \\
k_R = M_z / \theta_O = 2/P_2 + k_T L_{01}^2,
\end{cases}
\tag{12}
$$

where k_L, k_T and k_R are the longitudinal, transverse, and angular stiffness, respectively.

Substituting P_1–P_3 into Eq. (12), the in-plane stiffness of Structure I-III are obtained and provided in Table 1. It is found that the difference between the longitudinal and transverse stiffness is over 350 times. Therefore, these structures can be treated as rigid in the longitudinal direction. Table 1 also shows that Structure III is very

Table 1 In-plane stiffness of the SIS structures

	Longitudinal k_L /(N/μm)	Transverse k_T /(N/μm)	Rotational k_R /(N·m/rad)
SIS I	17.49	4.350×10^{-2}	23.53
SIS II	18.54	5.182×10^{-2}	26.72
SIS III	254.7	39.14	3.170×10^3

stiff in the longitudinal and transverse directions. Thus, Structure III can be treated as an ideal revolute joint.

3.3 Stress Concentration of the SIS Structure

In Section 3.2, an SIS structure can be treated as rigid in the longitudinal direction. Thus, the normal stress caused by the axial load is not investigated herein. During the lateral deformations, the normal stress caused by the bending effect is the dominant stress. Thus, the maximum stress locates on the outer surface of the hinge. The maximum stress on the outer surfaces can be expressed using the following equation:

$$
\sigma_{\max}(x) = -k_b \sigma_n(x) = -\frac{k_b y(x) M_z(x)}{I_z(x)} = -\frac{3k_b M_z(x)}{2dy^2(x)},
\tag{13}
$$

where k_b is the stress concentration factor for bending, $\sigma_{\max}$ and σ_n are the actual and nominal maximum stresses, respectively. For the leaf hinges in Structure I and II, the stress concentration has little influence on the bending compliance calculation according to DU's work [29]. As a result, k_b can be set to 1 for Structure I and II. For circular hinges in Structure III, according to the generalized model established in CHEN's work [30], the stress concentration factor is calculated to be 1.030.

Due to the symmetry, hinge 1 is selected to calculate the maximum stress. Based on Figure 3, the inner moment at position x_1 within hinge 1 is

$$
M_z(x_1) = M_{Az} + F_{Ay}(L_0 + x_1), \quad x_1 \in [-L_0, L_0].
\tag{14}
$$

Substituting Eqs. (10)–(12) into Eq. (14), the relationship between $M_z(x_1)$ and the SIS structure's deflections is

$$
M_z(x_1) = \frac{k_T[(L_0 + L_1)\theta_O - v_O]x_1}{2} + \frac{\theta_O}{P_2}, \quad x_1 \in [-L_0, L_0].
\tag{15}
$$

In this manipulator, Structure I and II act as prismatic joints, i.e., $\theta_O = 0$. In this case, substituting Eqs. (1) and (15) into Eq. (13), the following relationship is established:

$$
\frac{\sigma_x(x_1)}{v_O} = \frac{3k_b k_T x_1}{dt^2}, \quad x_1 \in [-L_0, L_0].
\tag{16}
$$

Qin *et al. Chin. J. Mech. Eng.* (2018) 31:7

Page 5 of 11

On the other hand, Structure III functions as a revolute joint, and thus $v_O = 0$. Substituting Eqs. (2) and (15) into (13), the relationship between the σ_x and v_O is established:

$$\frac{\sigma_x(x_1)}{\theta_O} = \frac{-3k_b[k_T(L_0 + L_1)P_2x_1 + 2]}{4dP_2\left(r + t/2 - r\sqrt{1 - x_1^2/r^2}\right)^2},$$
$$x_1 \in [-L_0, L_0]. \quad (17)$$

Eqs. (16) and (17) are utilized to obtain the maximum allowable deflections of the SIS structure. For Structure I and II, Eq. (16) shows that the maximum stress locates at both ends of the hinge. For Structure III, the location of the maximum stress can be obtained by differentiating Eq. (17) to x_1. Taking the yield strength of the material into consideration, the maximum allowable deflections of Structure I-III are calculated to be 1.46 mm, 1.30 mm, and 5.349 mrad, respectively.

4 Statics and Dynamics Modeling

Monolithic flexure-based mechanisms exhibit friction-less motions, resulting in an extremely low damping ratio. Hence, the nano-manipulator can be approximated as an undamped system. Based on Lagrange's equation, the dynamics of a system can be expressed as follows:

$$\frac{d}{dt}\left(\frac{\partial T}{\partial \dot{q}_i}\right) - \frac{\partial T}{\partial q_i} + \frac{\partial V}{\partial q_i} = Q_i, \quad i = 1, 2, \ldots, N, \quad (18)$$

where T and V denote the total kinetic and potential energy of the system, respectively; q_i and Q_i are the ith generalized coordinate and non-conservative force, respectively; and N is the number of generalized coordinates.

The first three modes of the nano-manipulator are the linear motions in the x- and y-axes and the angular motion about the z-axis. The linear motions in each axis are the primary motions, whereas the angular motion about the z-axis is an unexpected motion degrading the motion accuracy. In this section, the dynamics models in both linear and angular motions are established.

4.1 Influence of the lever's compliance

The lever in flexure-based mechanisms is typically treated as a rigid element [26, 27, 31] to facilitate the modeling process. This approximation may affect the estimated parameters of the overall system, e.g., the displacement amplification ratio. Figure 4(a) examines the lateral deformations of the lever in the nano-manipulator when a lateral force is applied at the free end. The contribution of Structure III is equivalent to a revolute joint with a torsional stiffness of k_{R3}. If the lever is assumed to be rigid, the free end moves to point C'. However, the lever is flexible, and the actual position of the free end is point
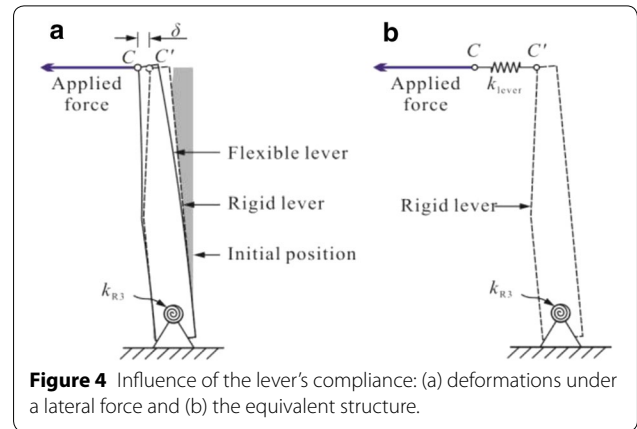

Figure 4 Influence of the lever's compliance: (a) deformations under a lateral force and (b) the equivalent structure.

C, with a distance of δ to point C'. The distance δ is negligible in very short levers while it becomes noticeable in long levers. In this paper, the equivalent structure shown in Figure 4(b) is proposed to account for the lever's compliance, where k_{lever} is the equivalent lateral stiffness of the lever with "clamped-free" boundary conditions. The modeling of k_{lever} is straightforward using the mechanics of materials, and thus it is omitted for the conciseness of this paper. In the lever mechanism, k_{lever} is calculated to be 1.111 N/μm.

Figure 5(a) shows the deformation of the manipulator in the x-axis, where linkages 2 and 4 remain stationary, and the central platform, linkages 1 and 3 generate the same displacement. This corresponds to the first/second mode. The masses of the central platform, linkages 1 and 3 are denoted as m_0, m_1, and m_3, respectively. In the contact interface, point A is the end of the PEA and point B represents the contact point on the lever. The lumped mass model in the x-axis can be depicted in Figure 5(b), where m_L is the load mass, and I_{lever} denotes the moment of inertia of the lever. In Figure 5(b), the equivalent
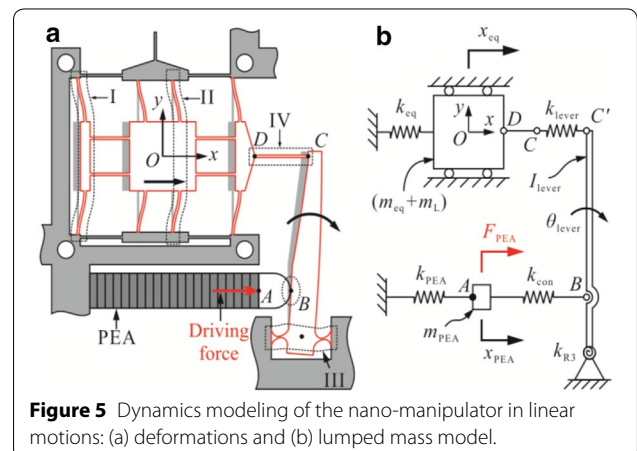

Figure 5 Dynamics modeling of the nano-manipulator in linear motions: (a) deformations and (b) lumped mass model.

Qin *et al. Chin. J. Mech. Eng.* (2018) 31:7

Page 6 of 11

stiffness and the effective mass of the central platform are defined in the following equation:

$$\begin{cases} k_{eq} = 2(k_{T1} + k_{T2}), \\ m_{eq} = m_0 + m_1 + m_3. \end{cases} \tag{19}$$

From the static and dynamic point of view, the PEA is equivalent to an active force generator. In Figure 5(b), the equivalent stiffness, the driving force, and the effective mass of the PEA are denoted as k_{PEA}, F_{PEA}, and m_{PEA}, respectively; and k_{con} represents the equivalent contact stiffness of the contact interface. Further, a dimensionless parameter, $\eta = k_{con}/k_{PEA}$, is proposed to characterize the contact stiffness. Three generalized coordinates are defined in Figure 5(b), namely, the displacement of the PEA (x_{PEA}), the rotation angle of the lever (θ_{lever}), and the linear displacement of the central platform (x_{eq}).

In this nano-manipulator, the connection between the PEA and the lever is not firm, and preload force is utilized to keep the PEA and the lever in contact. The input stiffness k_{in} is defined as the linear stiffness at point B when no PEA is installed. If k_{in} is too low or the preload force is not large enough, the detachment phenomenon may occur in large step motions. However, if the input stiffness is too high, the displacement of the PEA will be significantly reduced. Based on Figure 5(b), k_{in} can be calculated as follows:

$$k_{in} = \frac{k_{eq}k_{lever}}{k_{eq} + k_{lever}} \cdot \frac{h_3^2}{h_2^2} + \frac{k_{R3}}{h_2^2}. \tag{20}$$

The output stiffness is the linear stiffness of the central platform in the x or y axis that can be modeled as

$$k_{out} = k_{eq} + \frac{\left(\frac{\eta}{1+\eta}h_2^2 k_{PEA} + k_{R3}\right)k_{lever}}{\frac{\eta}{1+\eta}h_2^2 k_{PEA} + k_{R3} + h_3^2 k_{lever}}. \tag{21}$$

The displacement amplification ratio of the lever mechanism is the ratio between the displacements of points C and B, which can be expressed as

$$k_{amp} = \frac{x_{eq}}{h_2\theta_{lever}} = \frac{h_3}{h_2} \cdot \frac{k_{lever}}{k_{lever} + k_{eq}}. \tag{22}$$

The influence of the lever's compliance is significant. If the lever is assumed to be rigid, k_{lever} converges to infinity. In this case, k_{in}, k_{out}, and k_{amp} will be overestimated. On the contrary, if the lever's compliance is considered, the modeling complexity will increase significantly. Therefore, a criterion is necessary to to decide whether the lever's compliance can be neglected or not. Based on Eqs. (20)–(22), k_{lever} can only be neglected if the following two conditions are satisfied:

$$\begin{cases} k_{lever} > 100k_{eq}, \\ h_3^2 k_{lever} > 100\left(h_2^2 k_{PEA} + k_{R3}\right). \end{cases} \tag{23}$$

Eq. (23) is the criterion to decide whether the lever can be treated as rigid or not. In this nano-manipulator, $k_{lever} = 11.7k_{eq}$ and $h_3^2 k_{lever} = 0.618(h_2^2 k_{PEA} + k_{R3})$. As a result, the lever's compliance must be considered.

4.2 Dynamics of the Nano-manipulator in the *x*-axis

Based on Figure 5(b), the total kinematic and potential energy of the nano-manipulator are given below:

$$T = \tfrac{1}{2}m_{PEA}\dot{x}_{PEA}^2 + \tfrac{1}{2}I_{lever}\dot{\theta}_{lever}^2 + \tfrac{1}{2}\left(m_{eq} + m_L\right)\dot{x}_{eq}^2. \tag{24}$$

$$V = \tfrac{1}{2}k_{PEA}x_{PEA}^2 + \tfrac{1}{2}\eta k_{PEA}(h_2\theta_{lever} - x_{PEA})^2 + \tfrac{1}{2}k_{R3}\theta_{lever}^2 + \tfrac{1}{2}k_{lever}\left(h_3\theta_{lever} - x_{eq}\right)^2 + \tfrac{1}{2}k_{eq}x_{eq}^2. \tag{25}$$

Substituting Eqs. (24) and (25) into Eq. (18), the nano-manipulator's equations of motion in the *x*-axis are established as follows:

$$M\ddot{x} + Kx = u, \tag{26}$$

where

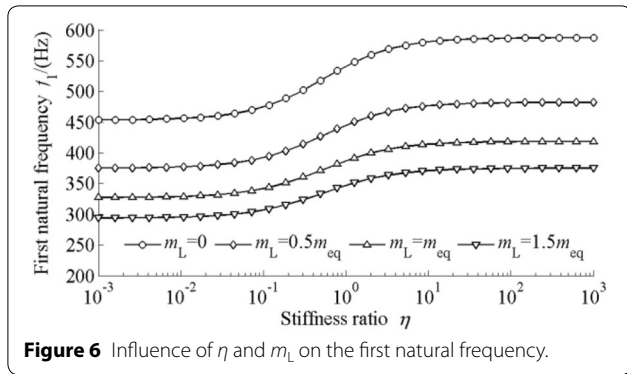$$M = \begin{bmatrix} m_{PEA} & 0 & 0 \\ 0 & I_{lever} & 0 \\ 0 & 0 & m_{eq} + m_L \end{bmatrix},$$

$$K = \begin{bmatrix} (1+\eta)k_{PEA} & -\eta h_2 k_{PEA} & 0 \\ -\eta h_2 k_{PEA} & \eta h_2^2 k_{PEA} + k_{R3} + h_3^2 k_{lever} & -h_3 k_{lever} \\ 0 & -h_3 k_{lever} & k_{lever} + k_{eq} \end{bmatrix},$$

$$x = [x_{PEA}, \theta_{lever}, x_{eq}]^T, \quad u = [F_{PEA}, 0, 0]^T. \tag{27}$$

There are three modal vibrations for the linear motions in the *x*-axis. The corresponding natural frequencies can be numerically obtained using

$$\left|K - \left(2\pi f_i\right)^2 M\right| = 0, \quad i = 1, 2, 3. \tag{28}$$

As the nano-manipulator is not designed as a high-speed scanner, only the first natural frequency is investigated, and all the higher order dynamics is neglected. The influence of the contact stiffness and the load mass on the first natural frequency is analyzed and shown in Figure 6. The variation range of η is 10^{-3} to 10^3, corresponding to the cases of low and high contact stiffness, respectively. When the contact stiffness is low, the first natural frequency converges to its lower bound, corresponding to the case when no PEA is installed. When the contact stiffness increases, the first natural frequency gradually converges to its upper bound. When $\eta > 100$, the first natural frequency starts to converge. This indicates that the contact interface can be treated as rigid if $\eta > 100$. As the load mass increases the effective mass of

Qin *et al.* Chin. J. Mech. Eng. (2018) 31:7

Page 7 of 11

Figure 6 Influence of η and m_L on the first natural frequency.

Figure 7 Influence of the contact stiffness on the static parameters.

the nano manipulator, its influence is also obvious in Figure 6: the first natural frequency decreases when the load mass increases.

4.3 Static Analysis of the Nano-manipulator

In static modeling, the velocities and accelerations are zero. Substituting these into Eq. (26), we can solve for the static relationships between the outputs and the input of the nano-manipulator, as shown below:

$$
\begin{cases}
x_{\text{PEA}} = \frac{k_{\text{in}} + \eta k_{\text{PEA}}}{k_{\text{in}} + \eta(k_{\text{in}} + k_{\text{PEA}})} \cdot x_{\text{PEA0}}, \\
\theta_{\text{lever}} = \frac{\eta k_{\text{PEA}}}{k_{\text{in}} + \eta(k_{\text{in}} + k_{\text{PEA}})} \cdot \frac{x_{\text{PEA0}}}{h_2}, \\
x_{\text{eq}} = \frac{\eta k_{\text{PEA}} k_{\text{amp}}}{k_{\text{in}} + \eta(k_{\text{in}} + k_{\text{PEA}})} \cdot x_{\text{PEA0}}.
\end{cases}
\tag{29}
$$

where $x_{\text{PEA0}} = F_{\text{PEA}}/k_{\text{PEA}}$ is defined as the nominal displacement of the PEA (free extension without loads).

In order to investigate the influence of the contact stiffness on the nano-manipulator's static characteristics, the following three dimensionless ratios are introduced to characterize the actual displacement of the PEA, the displacement applied to the lever, and the displacement of the central platform, respectively:

$$
g_1(\eta) = \frac{x_{\text{PEA}}}{x_{\text{PEA0}}}, \; g_2(\eta) = \frac{h_2 \theta_{\text{lever}}}{x_{\text{PEA0}}}, \; g_3(\eta) = \frac{x_{\text{eq}}}{x_{\text{PEA0}}}.
\tag{30}
$$

As Figure 7 illustrates, if the contact stiffness is low, g_1 converges to its upper bound of 1, and both g_2 and g_3 converge to zero. As a result, the majority of the PEA's displacement is not transmitted to the lever, but consumed in the contact interface. In contrast, if the contact stiffness is high, both g_1 and g_2 converge to $k_{\text{PEA}}/(k_{\text{in}}+k_{\text{PEA}})$, and g_3 converges to its upper bound of $k_{\text{PEA}}k_{\text{amp}}/(k_{\text{in}}+k_{\text{PEA}})$. Therefore, in practice, it is desirable to improve the contact stiffness so as to achieve larger workspace.

4.4 Angular Motion of the Nano-manipulator

As illustrated in Figure 8(a), when a moment M_z is applied on the central platform, the central platform and all the linkages experience almost the same rotations,
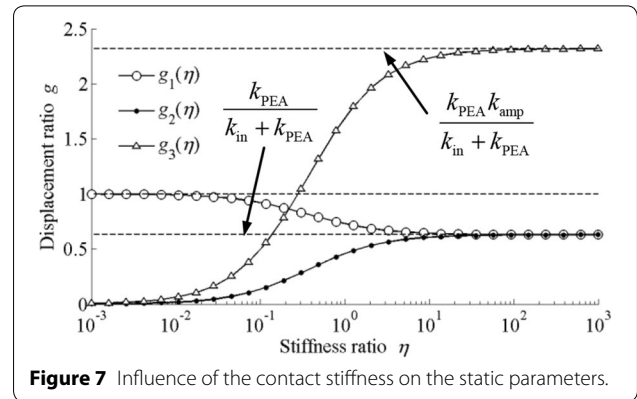
denoted as θ_{eq}. Figure 8(a) actually shows the third mode of the nano-manipulator. Based on the computational analysis, the lever mechanisms are almost stationary. Thus, this angular motion of the central platform has no effect on the PEAs, and the installations of the PEAs will not affect the angular behavior of the central platform.

The effective moment of inertia of the central platform, linkages 1 and 3 are denoted as I_0, I_1, and I_3, respectively. The corresponding rotation centers of linkages 1–4 are labeled as O_i (i = 1–4). During the angular motion, the load mass will increase the central platform's moment of inertia. If the load mass is assumed to be distributed uniformly across the central platform, the total kinematic energy of the nano-manipulator can be written as

$$
T = \frac{1}{2}[I_0 + I_L + 2(I_1 + I_3)]\dot{\theta}_{\text{eq}}^2,
\tag{31}
$$

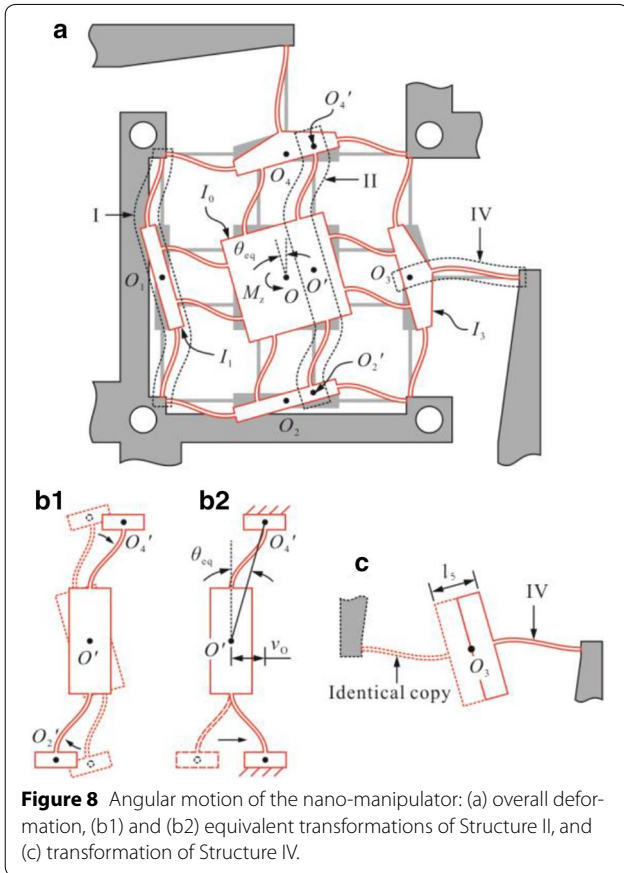where $I_L \approx m_L I_0 / m_0$ is the moment of inertia of the load mass.

For Structure I, the deformation is a rotation about the z-axis. The deformation of Structure II is separated and illustrated with dashed lines in Figure 8(b1). The respective rotation centers are labeled as O', O_2', and O_4'. Since the leaf springs and linkages are connected in parallelogram configurations, during the angular motion, the distance between points O' and O_4' is constant and equal to the distance between points O and O_4:

$$
\left| O'O_4' \right| = |OO_4| = (t_3 + 2l_2 + l_3)/2.
\tag{32}
$$

In Figure 8(b1), solid lines show a transformed structure obtained by counter rotating Structure II by an angle of $-\theta_{\text{eq}}$. A further transformation is illustrated in Figure 8(b2): flipping the deformation of the lower flexure hinge. The above operations do not change the potential energy of Structure II. Thus, the angular deformation of Structure II is transformed to a linear deformation v_O. The relationship between v_O and θ_{eq} can be established based on the geometric constraints as below:

$$
v_O = \left| O'O_4' \right| \cdot \sin(\theta_{\text{eq}}) \approx |OO_4|\theta_{\text{eq}}.
\tag{33}
$$

Qin *et al. Chin. J. Mech. Eng.* (2018) 31:7

Page 8 of 11

As illustrated in Figure 8(a), Structure IV rotates about point O_3 during the angular motion. If an identical copy of Structure IV is connected to the opposite side, a new structure is obtained, as shown in Figure 8(c). The topology of the new structure is the same as SIS I. The

Figure 8 Angular motion of the nano-manipulator: (a) overall deformation, (b1) and (b2) equivalent transformations of Structure II, and (c) transformation of Structure IV.

deformation is an angular displacement of θ_{eq} about the z-axis.

Based on the above analyses, the total potential energy of the nano-manipulator is derived as follows:

$$
\begin{aligned}
U &= 4\left[k_{R1}\theta_{eq}^2 \Big/ 2 + k_{T2}\left(|OO_4|\theta_{eq}\right)^2 \Big/ 2\right] + k_{R4}'\theta_{eq}^2 \Big/ 2 \\
&= \left(4k_{R1} + 4k_{T2}|OO_4|^2 + k_{R4}'\right)\theta_{eq}^2 \Big/ 2,
\end{aligned}
\tag{34}
$$

where k_{R4}' is the angular stiffness of the new structure in Figure 8(c). In this manipulator, $l_5 = 12.32$ mm. Utilizing Eq. (12), we have $k_{R4}' = 7.272$ N·m·rad^{-1}. Substituting Eqs. (31) and (34) into Eq. (18), the nano-manipulator's equations of motion about the z-axis is established to be

$$
\begin{aligned}
&[I_0 + I_L + 2(I_1 + I_3)]\ddot{\theta}_{eq} \\
&\quad + \left(4k_{R1} + 4k_{T2}|OO_4|^2 + k_{R4}'\right)\theta_{eq} = M_z.
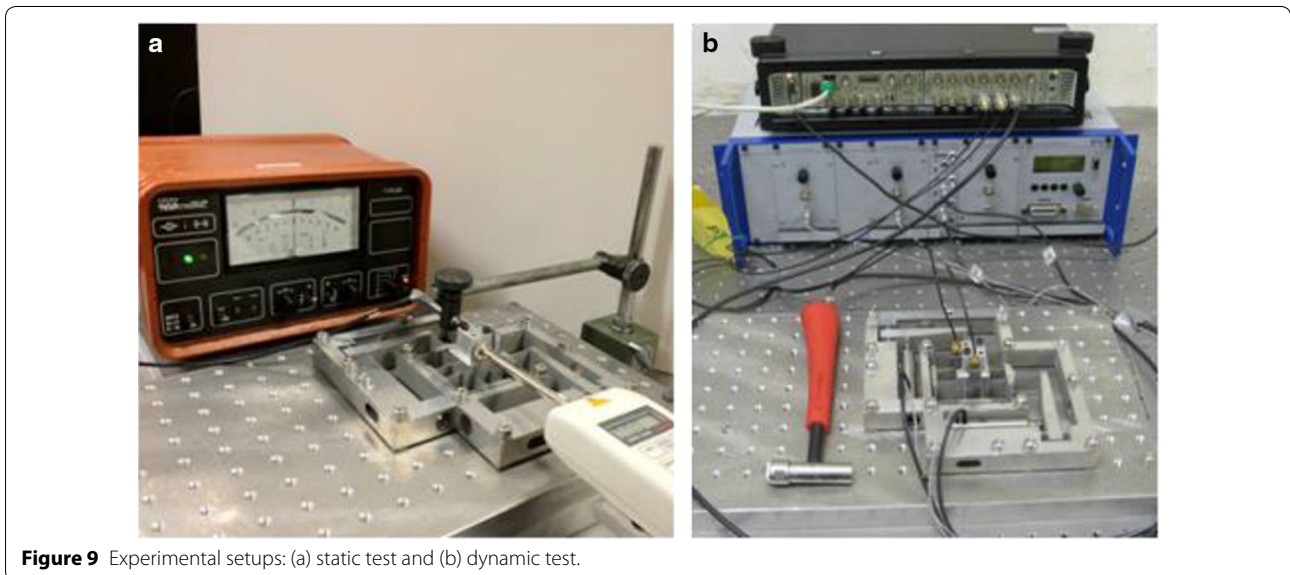\end{aligned}
\tag{35}
$$

Accordingly, the third natural frequency of the nano-manipulator can be calculated using

$$
f_3 = \frac{1}{2\pi}\sqrt{\frac{4k_{R1} + 4k_{T2}|OO_4|^2 + k_{R4}'}{I_0 + I_L + 2(I_1 + I_3)}}.
\tag{36}
$$

5 Experimental Verification
5.1 Experimental Setups
The static and dynamic characteristics of the nano-manipulator are experimentally investigated to verify the established models. Figure 9(a) shows the experimental setup for the static test, where the applied force and the resultant displacement of the central platform are measured. This corresponds to the output stiffness. The applied force is measured by a force gauge (HF-10 from

Figure 9 Experimental setups: (a) static test and (b) dynamic test.

Qin *et al. Chin. J. Mech. Eng.* (2018) 31:7

Page 9 of 11

ALGOL), and the displacement is measured using a displacement probe (GT21 from TESA Technology). Figure 9(b) shows the experimental setup for the dynamic test, where a modal hammer (ENDEVCO 2301-10 from MEGGITT) is used to excite the nano-manipulator, and the response is measured by two accelerometers (4507B from Brüel & Kjær) installed on the central platform.

During the experimental tests, the parameters of the nano-manipulator with and without the PEAs installed are measured individually. In the installations of the PEAs, each PEA is bolt-fixed on the nano-manipulator, and the preload force is manually adjusted. Based on the previous analyses, higher contact stiffness is preferred during the installation. The load mass is not measured in the static test because it has no influence on the static parameters of the nano-manipulator. In the dynamic test, the load mass is measured to be 53.4 g, including the fixtures and two accelerometers.

5.2 Statics of the Nano-manipulator

The measured and estimated output stiffness of the nano-manipulator are listed in Table 2. If no PEA is not installed, the analytical results are obtained by substituting $k_{PEA} = 0$ and $\eta = 0$ into Eq. (21). In this case, the estimation error of the analytical model (Analytical 1) is only -2%. If the PEAs are installed, the output stiffness of the nano-manipulator increases. As η is an unknown variable, the lower and upper bounds of the analytical results are provided. The measured output stiffness in each axis is close to the upper bound of the analytical results, indicating that high contact stiffness is achieved.

In order to investigate the influence of the lever's compliance, the analytical results with rigid lever assumption (Analytical 2) are also presented in Table 2 for the comparison. These analytical results are obtained by assigning k_{lever} a large value according to the criterion defined in Eq. (23). When no PEA is installed, the estimation error with rigid lever assumption is 42%. Such a high overestimation is not acceptable.

5.3 Dynamics of the Nano-manipulator

The frequency responses of the nano-manipulator are presented in Figure 10. Only the experimental results in the *x*-axis are presented due to the symmetry of the nano-manipulator. There are three peaks in the magnitude plot.
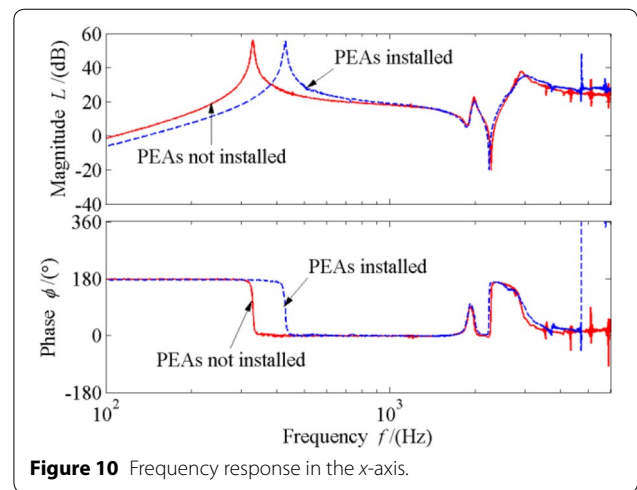

Figure 10 Frequency response in the *x*-axis.

The first peak corresponds to the first (or second) mode and the other two peaks are the unmodeled higher order dynamics. It is clearly illustrated that the installation of the PEAs only increases the first natural frequency.

The first natural frequencies in the *x*- and *y*-axes are given in Table 3. Without the PEAs, the first natural frequency in the *x*-axis is measured to be 320 Hz. If the lever's compliance is taken into consideration (Analytical 1), the estimation errors in the *x*-axis is 3.3%. When the PEAs are installed, the first natural frequency in the *x*-axis increase to 429 Hz. In this case, the lower and upper bounds of the analytical result are listed in Table 3. The measured first natural frequency is very close to the upper bound of the analytical result. This also demonstrates that high contact stiffness is achieved. Similarly, if the lever is assumed to be rigid (Analytical 2), the modeling accuracy is significantly affected. When no PEA is installed, the estimation error is 20.9%.

In current experimental setup, the third mode (rotations about the *z*-axis) doesn't show up in the measured data. Therefore, the computational analysis is employed to evaluate the nano-manipulator's behavior during the angular motions. Based on the computational results, the third natural frequency with the 53.4 g load mass is found to be 769.2 Hz. The analytical result is 754.1 Hz, corresponding to an estimation error of 2%, and thus validating the analytical model.

Table 2 Output stiffness in the *x*-axis

	Measured (N/µm)	Analytical 1 (N/µm)	Analytical 2 (N/µm)
No PEA	0.50	0.49	0.71
PEA installed	0.74	0.49–0.78	0.71–1.89

Table 3 First natural frequencies in the *x*-axis

	Measured (Hz)	Analytical 1 (Hz)	Analytical 2 (Hz)
No PEA	320	330.5	387.0
PEA installed	429	330.5–422.9	387.0–631.8

Qin *et al. Chin. J. Mech. Eng.* (2018) 31:7

Page 10 of 11

6 Conclusions

1. An XY flexure-based nano-manipulator is presented in this paper. Two PEAs are employed to generate actuations and the cross-axis couplings are attenuated in the kinematic chains. The flexure hinges, arranged in SIS configurations, function as prismatic and revolute joints. Lever mechanism is utilized to magnify the displacement of the PEA. It is found that the lever's compliance may significantly affect the estimated parameters of the nano-manipulator, such as the input/output stiffness and the first natural frequency. In this paper, a criterion is proposed to decide whether the lever's compliance can be neglected or not. The lever's compliance can be modeled by cascading a linear spring at the end of the lever. Although simple in formulation, this methodology is effective in improving the modeling accuracy, as verified through experimental results.

2. The dynamics of the nano-manipulator in linear and angular motions is analyzed. The influence of the contact stiffness and the load mass is analytically investigated. Higher contact stiffness results in improved performances, such as larger workspace and higher first natural frequency. The influence of the load mass is also significant as it adds extra inertia to the nano-manipulator.

3. The nano-manipulator is monolithically fabricated using wire electrical discharge machining technique. During the installation of the PEAs, the preload forces of the PEAs are manually tuned for a high contact stiffness. The analytical results show good modeling accuracy in comparison with the experimental results, and thus verifying the established models. The methodologies proposed in this paper are applicable in the design and optimization of flexure-based mechanisms.

Authors' contributions
YDQ designed the prototype, carried out the experiments and wrote the paper. XZ participated in the revision of the paper. BS participated in the design of experiments and revision of the paper. YLT and DWZ participated in the mechical design and manufacture of the prototype. All authors read and approved the final manuscript.

Author details
[1] Institute of Robotics and Automatic Information System (Tianjin Key Laboratory of Intelligent Robotics), Nankai University, Tianjin 300350, China. [2] Robotics and Mechatronics Research Laboratory, Department of Mechanical and Aerospace Engineering, Monash University, Clayton, VIC 3800, Australia. [3] School of Mechanical Engineering, Tianjin University, Tianjin 300072, China.

Authors' Information
Yan-Ding Qin is currently an associate professor at *Institute of Robotics and Automatic Information System, Nankai University, China*. He received his PhD degree from *Tianjin University, China*, in 2012. His research interests include micro/nano manipulation and 3D bio-printing.

  Xin Zhao is currently a professor at *Institute of Robotics and Automatic Information System, Nankai University, China*. He received PhD degree from *Nankai University, China*, in 1997. His research interests include micro operation robotics, MEMS, and biological pattern and tissue formation.

  Bijan Shirinzadeh is currently a professor at *Department of Mechanical and Aerospace Engineering, Monash University, Australia*. He received his PhD degree from *The University of Western Australia, Australia*, in 1990. His research interests include micro/nano manipulation, systems kinematics and dynamics, haptics and robotic-assisted surgery and microsurgery, and advanced manufacturing.

  Yan-Ling Tian is currently a professor at *School of Mechanical Engineering, Tianjin University, China*. He received his PhD degree from *Tianjin University, China*, in 2005. His research interests include micro/nano manipulation, mechanical dynamics, surface metrology and characterization

  Da-Wei Zhang is currently a professor at *School of Mechanical Engineering, Tianjin University, China*. He received his PhD degree from *Tianjin University, China*, in 1995. His research interests include micro/nano positioning techniques, high speed machining methodologies, and dynamic design of machine tools.

Publisher's Note
Springer Nature remains neutral with regard to jurisdictional claims in published maps and institutional affiliations.

References
1. D H Wang, Q Yang, H M Dong. A monolithic compliant piezoelectric-driven microgripper: design, modeling, and testing. *IEEE/ASME Transactions on Mechatronics*, 2013, 18(1): 138-147.
2. Y Qin, B Shirinzadeh, Y Tian, et al. Design issues in a decoupled XY stage: static and dynamics modeling, hysteresis compensation, and tracking control. *Sensors and Actuators A: Physical*, 2013, 194: 95-105.
3. T Secord, H H Asada. A variable stiffness PZT actuator having tunable resonant frequencies. *IEEE Transactions on Robotics*, 2010, 26(6): 993-1005.
4. H Tang, Y Li. Design, analysis, and test of a novel 2-DOF nanopositioning system driven by dual mode. *IEEE Transactions on Robotics*, 2013.
5. H Liu, J Wen, Y Xiao, et al. In situ mechanical characterization of the cell nucleus by atomic force microscopy. *ACS Nano*, 2014, 8(4): 3821-3828.
6. Y Qin, Y Tian, D Zhang, et al. A novel direct inverse modeling approach for hysteresis compensation of piezoelectric actuator in feedforward applications. *IEEE/ASME Transactions on Mechatronics*, 2013, 18(3): 981-989.
7. M Pellegrino, P Orsini, M Pellegrini, et al. Integrated SICM-AFM-optical microscope to measure forces due to hydrostatic pressure applied to a pipette. *Micro and Nano Letters*, 2012, 7(4): 317-320.
8. S Ryu, R Kawamura, R Naka, et al. Nanoneedle insertion into the cell nucleus does not induce double-strand breaks in chromosomal DNA. *Journal of Bioscience and Bioengineering*, 2013, 116(3): 391-396.
9. K Kuhnen. Modeling, identification and compensation of complex hysteretic and log(t)-type creep nonlinearities. *Control and Intelligent Systems*, 2005, 33(2): 134-147.
10. W T Ang, P K Khosla, C N Riviere. Feedforward controller with inverse rate-dependent model for piezoelectric actuators in trajectory-tracking applications. *IEEE/ASME Transactions on Mechatronics*, 2007, 12(2): 134-142.
11. M Szymonski, M Targosz-Korecka, K E Malek-Zietek. Nano-mechanical model of endothelial dysfunction for AFM-based diagnostics at the cellular level. *Pharmacological Reports*, 2015, 67(4): 728-735.

Qin *et al. Chin. J. Mech. Eng.* (2018) 31:7

Page 11 of 11

12. F Iwata, M Adachi, S Hashimoto. A single-cell scraper based on an atomic force microscope for detaching a living cell from a substrate. *Journal of Applied Physics*, 118, 134701 (2015), http://dx.doi.org/10.1063/1.4931936.

13. J M Paros, L Weisbord. How to design flexure hinges. *Machine Design*, 1965, 37(27): 151-156.

14. Y Li, Q Xu. Development and assessment of a novel decoupled XY parallel micropositioning platform. *IEEE/ASME Transactions on Mechatronics*, 2010, 15(1): 125-135.

15. H C Liaw, B Shirinzadeh, J Smith. Robust neural network motion tracking control of piezoelectric actuation systems for micro/nanomanipulation. *IEEE Transactions on Neural Networks*, 2009, 20(2): 356-367.

16. Y Li, Q Xu. Design and analysis of a totally decoupled flexure-based XY parallel micromanipulator. *IEEE Transactions on Robotics*, 2009, 25(3): 645-657.

17. L J Lai, G Y Gu, L M Zhu. Design and control of a decoupled two degree of freedom translational parallel micro-positioning stage. *Review of Scientific Instruments*, 2012, 83(4): 045105-1-17.

18. B J Kenton, K K Leang. Design and control of a three-axis serial-kinematic high-bandwidth nanopositioner. *IEEE/ASME Transactions on Mechatronics*, 2012, 17(2): 356-369.

19. Y K Yong, T F Lu, D C Handley. Review of circular flexure hinge design equations and derivation of empirical formulations. *Precision Engineering*, 2008, 32(2): 63-70.

20. Y Li, Q Xu. Modeling and performance evaluation of a flexure-based XY parallel micromanipulator. *Mechanism and Machine Theory*, 2009, 44(12): 2127-2152.

21. W O Schotborgh, F G M Kokkeler, H Tragter, et al. Dimensionless design graphs for flexure elements and a comparison between three flexure elements. *Precision Engineering*, 2005, 29(1): 41-47.

22. H C Liaw, B Shirinzadeh. Enhanced adaptive motion tracking control of piezo-actuated flexure-based four-bar mechanisms for micro/nano manipulation. *Sensors and Actuators A: Physical*, 2008, 147(1): 254-262.

23. Q Yao, J Dong, P M Ferreira. Design, analysis, fabrication and testing of a parallel-kinematic micropositioning *XY* stage. *International Journal of Machine Tools & Manufacture*, 2007, 47(6): 946-961.

24. Q Xu. New flexure parallel-kinematic micropositioning system with large workspace. *IEEE Transactions on Robotics*, 2012, 28(2): 478-491.

25. Y Qin, B Shirinzadeh, D Zhang, et al. Compliance modeling and analysis of the statically indeterminate symmetric flexure structure. *Precision Engineering*, 2013, 37(2): 415-424.

26. S B Choi, S S Han, Y M Han, et al. A magnification device for precision mechanisms featuring piezoactuators and flexure hinges: Design and experimental validation. *Mechanism and Machine Theory*, 2007, 42(9): 1184-1198.

27. Q Xu, Y Li, N Xi. Design, fabrication, and visual servo control of an XY parallel micromanipulator with piezo-actuation. *IEEE Transactions on Automation Science and Engineering*, 2009, 6(4): 710-719.

28. Y Qin, B Shirinzadeh, Y Tian. Design and computational optimization of a decoupled 2-DOF monolithic mechanism. *IEEE/ASME Transactions on Mechatronics*, 2014, 19(3): 872-881.

29. S W Han, S H Shin, S H Ryu, et al. Evaluation of DNA transcription of living cell during nanoneedle insertion. *Journal of Nanoscience and Nanotechnology*, 2016, 16(8): 8674-8677.

30. A J Mcdaid, K C Aw, S Q Xie, et al. Optimal force control of an IPMC actuated micromanipulator for safe cell handling. *Proceedings of the Proceedings of SPIE - The International Society for Optical Engineering, F*, 2012.

31. Y Tian, B Shirinzadeh, D Zhang. A flexure-based five-bar mechanism for micro/nano manipulation. *Sensors and Actuators A: Physical*, 2009, 153(1): 96-104.